

Instant polarized light microscopy pi (IPOL π) for quantitative imaging of collagen architecture and dynamics in ocular tissues

Po-Yi Lee^{1,2}, Hannah Schilpp², Nathan Naylor²,
Simon C. Watkins,³ Bin Yang⁴, Ian A Sigal^{1,2*}

¹ Department of Bioengineering, Swanson School of Engineering,

² Department of Ophthalmology, School of Medicine,

³ Department of Cell Biology, School of Medicine,
University of Pittsburgh, Pittsburgh, PA

⁴ Department of Engineering, Rangos School of Health Sciences,
Duquesne University, Pittsburgh, PA

Short Title: IPOL π for fast quantitative imaging of eye collagen

*** Correspondence:**

Ian A. Sigal, Ph.D.

Laboratory of Ocular Biomechanics

Department of Ophthalmology, University of Pittsburgh School of Medicine

203 Lothrop Street, Eye and Ear Institute, Room 930, Pittsburgh, PA 15213

Phone: (412) 864-2220; Fax: (412) 647-5880

Email: ian@OcularBiomechanics.com

www.OcularBiomechanics.com

Key Words: polarized light microscopy; collagen; biomechanics; optic nerve head

Disclosures: Nothing to disclose.

Funding: Supported in part by National Institutes of Health R01-EY023966, R01-EY031708, 1S10RR028478, P30-EY008098 and T32-EY017271 (Bethesda, MD), the Eye and Ear Foundation (Pittsburgh, PA), and Research to Prevent Blindness (unrestricted grant to UPMC ophthalmology, and Stein innovation award to Sigal, IA).

1 **Highlights**

2

3 • We introduce IPOL π , addressing IPOL limitations for characterizing eye collagen.

4 • IPOL π orientation-encoded color cycle is 180° (π radians) instead of 90° in IPOL.

5 • IPOL π requires a lower exposure time than IPOL, allowing faster imaging speed.

6 • IPOL π visualizes non-birefringent tissues and backgrounds from brightness.

7 • IPOL π is cheaper and less sensitive to imperfectly collimated light than IPOL.

8

9 **Abstract**

10 Collagen architecture determines the biomechanical environment in the eye, and thus
11 characterizing collagen fiber organization and biomechanics is essential to fully understand eye
12 physiology and pathology. We recently introduced instant polarized light microscopy (IPOL) that
13 encodes optically information about fiber orientation and retardance through a color snapshot.
14 Although IPOL allows imaging collagen at the full acquisition speed of the camera, with
15 excellent spatial and angular resolutions, a limitation is that the orientation-encoding color is
16 cyclic every 90 degrees ($\pi/2$ radians). In consequence, two orthogonal fibers have the same
17 color and therefore the same orientation when quantified by color-angle mapping. In this study,
18 we demonstrate IPOL π , a new variation of IPOL, in which the orientation-encoding color is
19 cyclic every 180 degrees (π radians). Herein we present the fundamentals of IPOL π , including a
20 framework based on a Mueller-matrix formalism to characterize how fiber orientation and
21 retardance determine the color. The improved quantitative capability of IPOL π enables further
22 study of essential biomechanical properties of collagen in ocular tissues, such as fiber
23 anisotropy and crimp. We present a series of experimental calibrations and quantitative
24 procedures to visualize and quantify ocular collagen orientation and microstructure in the optic
25 nerve head, a region in the back of the eye. There are four important strengths of IPOL π
26 compared to IPOL. First, IPOL π can distinguish the orientations of orthogonal collagen fibers
27 via colors, whereas IPOL cannot. Second, IPOL π requires a lower exposure time than IPOL,
28 thus allowing faster imaging speed. Third, IPOL π allows visualizing non-birefringent tissues and
29 backgrounds from tissue absorption, whereas both appear dark in IPOL images. Fourth, IPOL π
30 is cheaper and less sensitive to imperfectly collimated light than IPOL. Altogether, the high
31 spatial, angular, and temporal resolutions of IPOL π enable a deeper insight into ocular
32 biomechanics and eye physiology and pathology.

33

34 **1. Introduction**

35 Collagen is a primary load-bearing component in ocular tissues. Its architecture determines
36 the ocular biomechanical environment and susceptibility to several vision threatening conditions.
37 (Coudrillier et al., 2012; Ethier et al., 2004) Therefore, characterizing collagen fiber organization
38 and biomechanics is important to fully understand eye physiology and preventing vision loss.

39 Polarized light microscopy (PLM) has been used to study collagen architecture in soft
40 tissues for several decades. (Canham et al., 1991; Diamant et al., 1972; Keefe et al., 1997;
41 Tower et al., 2002) A major advantage of PLM over other more conventional histology is that it
42 does not require labels or stains, avoiding potential artifacts and simplifying preparation. (Koike-
43 Tani et al., 2015) Over the past few years widefield PLM has continued to be refined and
44 recently demonstrated robust for characterizing collagen architecture of posterior pole ocular
45 tissues. (Brazile et al., 2018; Filas et al., 2014; Gogola et al., 2018a; Gogola et al., 2018b; Jan
46 et al., 2018; Jan et al., 2017a; Jan and Sigal, 2018; Jan et al., 2015b; Jan et al., 2017c; Yang et
47 al., 2018a; Yang et al., 2018b) Other imaging techniques leveraging polarized light have also
48 been used extensively to study ocular collagen, including polarization sensitive second
49 harmonic generation (PS-SHG) (Cisek et al., 2021; Gusachenko et al., 2012; Mansfield et al.,
50 2008) and polarization sensitive optic coherent tomography (PS-OCT) (Baumann et al., 2014;
51 Willemse et al., 2020; Yamanari et al., 2014). Nevertheless, widefield PLM has several
52 strengths over raster-scanning techniques that continue to make it highly useful for soft tissues.
53 PLM produces images with high, micrometer-scale, resolution over wide regions at high imaging
54 speeds. PLM is substantially simpler and therefore cheaper. (Higgins, 2010; Whittaker and
55 Przyklenk, 2009) The high angular resolution and sub-pixel information of PLM allows accurate
56 measurement of small fiber undulations, or crimp. (Jan et al., 2015a; Kalwani et al., 2013) This
57 is of particular interest for the study of the relationship between tissue architecture and
58 biomechanics as it allows quantifying fiber crimp without the need to discern or trace individual
59 fibers. Fiber tracing is very demanding on image resolution and analysis time, often leading to a
60 reduced number of measurements. The above have made PLM a preferred technique for
61 measuring collagen crimp.

62 Conventional quantitative PLM, however, requires multiple images at different polarization
63 states to compute the collagen structure and orientation. (Shribak and Oldenbourg, 2003) Multi-
64 image acquisition not only limits the imaging speed to evaluate the static architecture or quasi-
65 static behavior in ocular tissues but may also introduce quantitative errors from post-processing
66 among images, such as image registration.

67 Instant polarized light microscopy (IPOL) is a recently introduced technique that optically
68 encodes information about fiber orientation and retardance through a color snapshot. (Lee et al.,
69 2022; Yang et al., 2021) IPOL allows quantitative imaging of collagen at the full acquisition
70 speed of the camera, with excellent spatial and angular resolutions. IPOL, however, has the
71 limitation that the orientation-encoded colors are cyclic every 90 degrees ($\pi/2$ radians). In
72 consequence, two orthogonal fibers have the same color and therefore the same orientation
73 when quantified by color-angle mapping. Techniques to distinguish the orientations of
74 orthogonal fibers have been suggested, (Keikhosravi et al., 2021) but the detailed methodology
75 to quantify orientation and retardance have not been described.

76 Our goal in this work was to demonstrate IPOL π , a new variation of IPOL, in which the
77 orientation-encoding color is cyclic every 180 degrees (π radians). We describe how to use
78 IPOL π to conduct quantitative analysis on static and dynamics of ocular tissues, with high
79 spatial and temporal resolutions. We present the fundamentals of IPOL π , including a framework
80 based on a Mueller-matrix formalism to characterize how fiber orientation and retardance
81 determine the color. The improved quantitative capability of IPOL π enables further study of
82 essential biomechanical properties of collagen in ocular tissues, such as fiber anisotropy and
83 crimp. We present a series of experimental calibrations and quantitative procedures to visualize
84 and quantify ocular collagen orientation and microstructure in the optic nerve head, a region in
85 the back of the eye.

86 2. Methods

87 This section is organized into five parts. In Section 2.1, we describe the configuration of
88 IPOL π imaging system. In Section 2.2, we introduce a framework based on a Mueller-matrix
89 formalism to characterize how the color changes in fiber orientation and retardance. This
90 simulation helps builds a foundation of quantitative analysis from the proposed imaging. In
91 Section 2.3, we demonstrate how to experimentally calibrate the relationship between color and
92 fiber orientation and the relationship between color and retardance. In Section 2.4, we introduce
93 how to use the interpolating functions obtained from the experimental calibration in Section 2.3
94 to quantify images acquired by IPOL π and then to visualize the quantitative results. Finally, in
95 Section 2.5, we demonstrate the applications of IPOL π for visualizing and quantifying static
96 collagen architecture and dynamic collagen deformation under uniaxial stretch testing of optic
97 nerve head tissues.

98 2.1 IPOL π imaging system

99 The optic design of IPOL π was to retrofit a commercial inverted microscope (Olympus IX83,
100 Olympus, Tokyo, Japan) with a white light source, circular polarizer, polarization decoder, and
101 color camera (DP74, Olympus, Tokyo, Japan) (**Figure 1**). Polarization decoder consists of a z-
102 cut quartz and a linear polarizer. In the absence of a birefringent sample, the spectrum of the
103 white light was unchanged and the image background appeared grey. With a birefringent
104 sample, such as collagen, the spectrum of the white light was changed and thus the light
105 appeared colorful. The frame rate of IPOL π was limited only by that of the color camera, which
106 in our setup was 60 frames per second.

107 2.2 IPOL π simulation

108 The polarization simulation was used to characterize the relationship between the output
109 RGB color from IPOL π and the material properties of collagen. We applied a Mueller-matrix
110 formalism to simulate how the polarization states of the broadband white-light spectrum were
111 altered through optical elements and a sample. In the Mueller-matrix formalism, briefly, a series
112 of 4x4 transfer matrices, i.e., Mueller matrices, was introduced to operate on an incident 1x4
113 Stokes vector to obtain the corresponding transmitted Stokes vector. (Collett, 2005) The Stokes
114 vector S_{out} of the output light from IPOL π can be described as

$$S_{out}(\varphi, \delta, \lambda) = M_{P(0^\circ)} \cdot M_{ROT}(\lambda) \cdot M_{sample}(\varphi, \delta) \cdot M_{QWP}(\lambda) \cdot M_{P(45^\circ)} S_{in}(\lambda) \quad (1)$$

115 where M were the Mueller matrices and S were the Stokes vectors. The spectrum of the
116 incident light S_{in} was referred to our LED white light source (IX3-LJLEDC, Olympus, Tokyo,
117 Japan). A linear polarizer M_P orientated at 45 degrees and a quarter waveplate was equivalent
118 to a circular polarizer. We simulated and compared the effects on the output light of four quarter
119 waveplates: ideal (i.e., wavelength independent), achromatic (AQWP05M-580, Thorlabs, NJ,
120 USA), zero-order (WPQ05ME-546, Thorlabs, NJ, USA), and multi-order (WPMQ05M-532,
121 Thorlabs, NJ, USA). A phase retarder, M_{sample} , was used to represent the birefringent sample,
122 such as collagen fibers, where the slow axis orientation α varying from 0 to 180 degrees, and
123 the retardance δ varying from 0 to π radians. A z-cut quartz was model as a polarization rotator,
124 M_{ROT} , where the rotated angles were wavelength dependent. The polarization rotator allowed
125 diverged the polarization directions of the visible spectrum (400-700 nm) within 180 degrees.
126 The last one was a linear polarizer, M_P , orientated at 0 degrees, also called an analyzer. For a
127 given fiber orientation and retardance, S_{out} was calculated for the wavelengths between 400nm
128 and 700 nm, where the first parameter of the 1×4 Stroke vector represented intensity. Each
129 wavelength had a corresponding RGB (Red, Green, Blue) value, an additive color model. The
130 RGB color was subsequently obtained by spectrally mixing the wavelength-dependent intensity
131 of the output. The simulated color was converted from the RGB color space to the HSV (Hue,
132 Saturation, Value) color space (Schanda, 2007). Note that the meanings of the terms “value”
133 and “brightness” were the same in this study.

134 **2.3 RGB color calibration**

135 With the understanding of the relationship between color and material properties of collagen
136 from the Section 2.2, we performed an experimental calibration and developed an algorithm to
137 build system-specific color-angle and color-energy conversion maps. A chicken Achilles tendon
138 was dissected and fixed with 10% formalin for 24 hours while under load. (Yang et al., 2018b;
139 Yang et al., 2021) Following fixation, the tendon was cryo-sectioned longitudinally into 20- μ m-
140 thick sections. The tendon section fixed while under load was considered a uniform collagen
141 organization with consistent fiber orientation. IPOL π images were acquired with the chicken
142 tendon section at several controlled angles relative to the longitudinal fiber direction, from 0 to
143 180 degrees, every 2 degrees.

144 Post-processing was necessary to extract the averaged color from the section and actual
145 rotation angles due to regional variations in fiber content and orientation and the limited
146 rotational accuracy. The individual images were registered and the rotation angles were
147 obtained from the transformation matrices using Fiji software. (Schindelin et al., 2012) Then,

148 with a region of interest manually placed on the color-uniform area in the stack, the RGB colors
149 were extracted and averaged from the region of interest from the corresponding frames. The
150 calibrated background was the mean of the colors obtained from all frames. The distance
151 between color on experimental calibration and calibrated background as a unit of “energy”,
152 which was related to retardance. We used the experimental calibration to generate pseudo
153 calibrations with corresponding orientations and energies (**Figure 2**). The energy in low-
154 brightness pseudo calibrations was weighted by the brightness to avoid image noise. We
155 interpolated a combination of pseudo and experimental calibrations to build interpolating
156 functions for orientation and energy inquiry. (Amidror, 2002)

157 **2.4 Quantification and visualization**

158 Fiber orientation and energy maps for all images were obtained by searching RGB values for all
159 pixels over the color-angle and color-energy interpolating functions, respectively, obtained from
160 Section 2.3. For visualization, the post-processed image was made from the orientation map of
161 the collagen fibers rendered by a HSV colormap and the brightness was weighted by the energy
162 map.

163 **2.5 Imaging collagen architecture and deformation**

164 *Sample preparation for static imaging.* A normal one-year-old sheep eye was obtained from
165 a local abattoir within four hours after death and formalin-fixed for 24 hours at 22 mmHg of
166 intraocular pressure. (Jan et al., 2015a) The muscles, fat, and episcleral tissues were carefully
167 removed. The optic nerve head region was isolated using an 11-mm-diameter trephine and
168 embedded in optimum cutting temperature compound (Tissue-Plus; Fisher Healthcare, TX,
169 USA).

170 *Sample preparation for uniaxial stretch testing.* An unfixed sheep eye section was prepared
171 as described in detail previously (Jan et al., 2022). Briefly, a normal one-year-old sheep eye
172 was obtained from a local abattoir within four hours after death. The muscles, fat, and episcleral
173 tissues were carefully removed. The optic nerve head region was isolated using an 11-mm-
174 diameter trephine and embedded in optimum cutting temperature compound (Tissue-Plus;
175 Fisher Healthcare, TX, USA). Samples were then snap frozen in liquid nitrogen-cooled
176 isopentane and sectioned coronally at a thickness of 16 μm . OCT was washed with multiple
177 PBS baths. To prevent curling or tears at the clamp points, a tissue section was sandwiched
178 between two pieces of silicone sheet (Medical Grade, 0.005”; BioPlexus, AZ, USA). The sheets
179 also allowed using PBS to maintain tissue hydration without lensing.

180 *Static imaging for optic nerve head collagen architecture.* Tissue samples were imaged
181 using IPOL π and IPOL with a 10x strain-free objective (numerical aperture [NA] = 0.3). Due to
182 the limited field of view of the objective, mosaicking was used to image the whole section. The
183 mosaics were obtained with 20% overlap and stitched using Fiji. (Schindelin et al., 2012)

184 *Dynamic imaging for sclera while under uniaxial stretching.* Each section was mounted to a
185 custom uniaxial stretching device and then stretched on both sides equally and dynamically.
186 The section was imaged using IPOL π with a 4x strain-free objective (NA = 0.13) to visualize a
187 sclera region. The frame rate was 60 frames per second. Angles within a scleral region were
188 extracted from the initial and three stretching states. Each two states had a 240-frame gap.

189

190 **3. Results**

191 **3.1 IPOL π simulation**

192 A simulated RGB color map of IPOL π presented the interaction with collagen fiber
193 orientation angles from 0 to 180 degrees and retardance from 0 to π radian (**Figure 3a**).
194 Although the colors looked like a continuous rainbow with orientations in the colormap, the
195 relationship of retardance to hue was not a constant and the relationship to brightness was not a
196 strictly increasing function (**Figure 3b**). Therefore, neither hue nor brightness was a suitable
197 parameter for quantifying collagen fiber orientation and retardance, particularly in low-
198 retardance tissues. In the RGB color space, the simulated result appeared as concentric circles,
199 where the radius increased with an increase in retardance (**Figure 3c**). In addition, a non-
200 birefringent sample was located at the central point of the circles. We found that the normalized
201 radius followed the sine function of the retardance, which was equivalent with what we have
202 called normalized “energy” in our previous studies. (Jan et al., 2015a; Jan et al., 2017b) (**Figure**
203 **3d**). The explanation of the relationship between the normalized radius and the energy is
204 addressed in more detail in the Discussion. Types of quarter waveplates to build IPOL π would
205 remarkably impact how the simulated curves within 180-degree orientation in the RGB color
206 space (**Figure 3e**).

207 **3.2 RGB color calibration**

208 Images of the chicken tendon section were acquired every 2 degrees from 0 to 180 degrees.
209 The color extracted from the images is presented in the RGB color space with a representative
210 subset of 8 images (**Figure 4a**). The color of the sample acquired by IPOL π depended on its
211 orientation. All colors formed an enclosing ring in the RGB color space, with the background
212 color located at the center of the ring. A combination of pseudo and experimental calibrations
213 was generated with the corresponding orientations (**Figure 4b**) and energies (**Figure 4c**).
214 These scatter points were used to build two interpolating functions that produced interpolated
215 orientations and energies, respectively, at inquiry RGBs. Note that these interpolating functions
216 are specific to our system. Other systems will potentially vary and therefore require calibration.

217 **3.3 Collagen architecture and deformation**

218 IPOL π allowed visualizing the collagen microstructure and orientation in high spatial and
219 angular resolutions (**Figure 5**). The raw image allowed identifying birefringent (e.g., collagen
220 and neural tissues) and non-birefringent (e.g., pigment, and background) components. Collagen
221 and neural tissues are easy to distinguish due to the large differences in birefringence. These

222 are, in part because of their composition, but also because the axons are primarily
223 perpendicular to the section and therefore have lower birefringence than the collagen fibers that
224 are primarily in the plane. (Axer et al., 2001; Yang et al., 2018b) Collagen fibers in the lamina
225 beams and in the scleral canal have clear differences in color, illustrating the strength of IPOL π
226 having color cycles every 180 degrees compared with conventional IPOL with color cycles every
227 90 degrees. This help distinguish fibers, even in dense sclera and in complex lamina beams.
228 The post-processed image shows collagen orientation quantitatively. This grey background or
229 region was converted into dark in the energy map. This enhanced the contrast between
230 birefringent and non-birefringent architecture. Figure 6a shows an example IPOL π image
231 mosaic of a coronal section of sheep optic nerve head. The post-processed image shows
232 orientation and energy information (**Figure 6b**), allowing further quantitative analysis at different
233 scales. At a large scale, IPOL π allows the calculation, for instance, of regional fiber anisotropy.
234 At a small scale, IPOL π allows identifying collagen microscale properties such as crimp, or the
235 natural waviness of collagen fibers, discernible in both the PPS and LC regions (**Figure 6c**).
236 IPOL π can capture dynamic deformations such as uniaxial stretch testing (**Figure 7a**). All post-
237 processing can be conducted after the testing (**Figure 7b**). High spatial and temporal
238 resolutions of IPOL π enabled the visualization and quantification of the process of load-induced
239 collagen fiber re-orientations (**Figure 7c**).

240

241 4. Discussion

242 Our goal was to demonstrate IPOL π , a new variation of IPOL in which the orientation-
243 encoding color is cyclic every 180 degrees (π radians). We have shown that IPOL π produces
244 color images with high spatial, angular and temporal resolutions, suitable for visualization and
245 quantitative analysis of the architecture and dynamics of optic nerve head tissues. Using
246 simulations we built a foundation to convert RGB color into orientation and energy information,
247 and have proved that the orientation-encoded color is cyclic every 180 degrees. The
248 quantitative capability of IPOL π enables further study on essential biomechanical properties of
249 collagen, such as fiber anisotropy and crimp. We have illustrated the application of IPOL π high
250 frame rates to show fiber reorientation in uniaxial stretch tests. Altogether, the high spatial and
251 temporal resolutions of IPOL π enable a deeper insight into ocular structure and biomechanics,
252 and through this on eye physiology and pathology. IPOL π combines features of conventional
253 PLM and IPOL and that we discuss in detail below. Interestingly, through this work we have also
254 shown that IPOL π has several convenient properties beyond the color cycle. Further down in
255 the discussion we address these, explaining the strengths and potential applications.

256 Both IPOL π and conventional PLM allow distinguishing fiber orientations ranging from 0 to
257 180 degrees since both system configurations include a circular polarizer that can differentiate
258 the polarization directions of light ranging from 0 to 180 degrees. (Jan et al., 2015a; Kalwani et
259 al., 2013) Images acquired using conventional PLM are monochromatic, and thus the selection
260 of the circular polarizer can be specific to the use of the imaging wavelength. In contrast, in
261 IPOL π , white light is used to acquire images. Since there is no ideal circular polarization (i.e.,
262 perfectly wavelength-independent), the output polarization of each wavelength other than the
263 specific wavelength through the circular polarizer is not ideal circular polarization. The ability of
264 the circular polarizer to minimize the difference in the output polarization of each wavelength
265 affects how the output color changes with collagen orientation, which further affects the
266 capability of distinguishing collagen orientation via color. In Figure 3E, we demonstrate IPOL π
267 configured with a circular polarizer made by an achromatic or zero-order quarter waveplate can
268 produce a clear color for visualization and quantification of collagen orientation.

269 Both IPOL π and conventional PLM allow quantifying the retardance of the collagen
270 structure. Conventional PLM requires images with different polarization states to derive
271 information such as fiber orientation and retardance (Jan et al., 2015a; Mehta et al., 2013). In

272 the four-frame algorithm without extinction setting, the measured retardance δ can be calculated
273 as (Shribak and Oldenbourg, 2003)

$$\delta = \sin^{-1} \left(\frac{2\sqrt{(I_{90^\circ} - I_{0^\circ})^2 + (I_{135^\circ} - I_{45^\circ})^2}}{I_{0^\circ} + I_{45^\circ} + I_{90^\circ} + I_{135^\circ}} \right). \quad (2)$$

274 where four intensity measurements, I_{0° , I_{45° , I_{90° , and I_{135° , are taken with linear polarizer analyzer
275 set to 0° , 45° , 90° , and 135° , respectively. We previously defined an “energy” for visualization as
276 (Jan et al., 2015a; Jan et al., 2017b)

$$energy = \sqrt{(I_{90^\circ} - I_{0^\circ})^2 + (I_{135^\circ} - I_{45^\circ})^2}. \quad (3)$$

277 From Equations 2 and 3, we know energy is the sine function of the retardance without
278 normalization. In Figure 3D, we found that the normalized RGB distance (i.e., radius) between
279 the calibrated color and calibrated background color followed the sine function of the
280 retardance. Therefore, it indicates the RGB distance is equivalent with “energy”.

281 IPOL π has faster imaging speed and preserves higher resolution than conventional PLM
282 due to the need in PLM of acquiring images with different polarization states. Imaging speed
283 limited by the time required to change the analyzer orientation often precludes conventional
284 PLM from applications on dynamic tissue deformation. (Tower et al., 2002) Several techniques
285 have been demonstrated to improve the imaging speed, such as multiplexing on a single image
286 sensor (Gruev et al., 2010; Kaminsky et al., 2007) and switching polarization states quickly
287 (Keikhosravi et al., 2017). However, these techniques still suffer from post-processing, i.e.,
288 image registration and denoising, which takes time and may introduce errors. The interpolation
289 for image registration may introduce errors in orientation and retardance calculations. For large
290 samples, mosaicking is required. Stitching among multiple views also interferes with image
291 registration in a single view, sometimes causing in a large error. Using a camera with built-in
292 multi-analyzer grids on the imaging sensor is a powerful solution for conventional PLM, which
293 acquires images with four polarization states in a snapshot (York et al., 2014). However, having
294 the analyzers integrated, such camera is limited in other applications where it would be
295 preferable to not have the analyzers. In IPOL π , placing z-cut quartz beside the analyzer allowed
296 diverging the polarization directions of the visible spectrum, generating a colorful light related to
297 collagen fiber microstructure and orientation. IPOL π only needs a color snapshot. Post-
298 processing is just for color inquiry at a single pixel and thus can be computed in parallel or after

299 imaging. Therefore, IPOL π preserves the original spatial and temporal resolution offered by the
300 imaging system.

301 Z-cut quartz induces different polarization rotations within the spectrum, thus affecting the
302 output spectrum and forming the color in IPOL π . Polarization rotation involves amount and
303 direction. The polarization rotation amount through z-cut quartz depends on the thickness of z-
304 cut quartz and the wavelength of the light. Thicker z-cut quartz increases the difference in
305 polarization rotation within the spectrum. To achieve IPOL π orientation-encoded color close to
306 “a hue color wheel” (red-yellow-green-blue-red), a suitable thickness of z-cut quartz is critical,
307 which causes enough polarization rotation differences (~180 degrees) in a visible spectrum.
308 Since the thickness of z-cut quartz is mm-level, the effects of parallelism and surface flatness on
309 polarization rotation difference can be ignored. The polarization rotation direction depends on
310 the handedness of z-cut quartz. Therefore, the handedness of z-cut quartz only affects whether
311 the IPOL π orientation-encoded color is in clockwise or counterclockwise order.

312 Both IPOL π and IPOL imaging techniques are based on z-cut quartz to modulate the
313 polarization directions of the visible spectrum, and thus can acquire different polarizations of
314 light via a snapshot. We note three similarities in imaging capability. First, both allow direct
315 visualization of collagen architecture in color. Second, both leverage the full spatial resolution of
316 the microscope-camera system since both use a single snapshot to acquire birefringent
317 information. Third, theoretically, both acquisition speeds are limited only by the camera, thus
318 both are suitable for imaging tissue dynamics and biomechanics.

319 The configuration of IPOL π includes a quarter waveplate but not in IPOL, resulting in
320 different imaging features. We highlight three important strengths of imaging capability of IPOL π
321 compared to the traditional 90-degree IPOL. First, the IPOL π image can identify the orientations
322 of orthogonal collagen fibers (e.g., laminar beams and collagen fibers in the scleral canal)
323 through colors since the orientation-encoded color in IPOL π was 180-degree cyclic. In IPOL π ,
324 when the circularly polarized light passes through the birefringent sample, the light becomes
325 elliptically polarized. The analyzer can distinguish the elliptically polarized light with orthogonal
326 axes. In contrast, the orientation-encoded color in IPOL is 90-degree cyclic. IPOL 90-degree
327 cyclic due to its crossed polarizer’s setup. In Malus’s Law, the output intensity of linearly
328 polarized light varies the square of the cosine (i.e., 90-degree cyclic) of the angle between the
329 polarization angle and the transmission axes of the analyzer. Second, acquiring a IPOL π image
330 only required 1/100 exposure time than acquiring a conventional IPOL image, thus allowing

331 faster imaging speed. The conventional IPOL includes a cross-polarizer design. The design
332 causes a dark background and also causes a low optical transmission rate except for
333 birefringent regions with high retardance. In contrast, a combination of a circular polarizer and
334 an analyzer in IPOL π does not block the light, and thus the optical transmission rate is high,
335 independent of retardance. Third, IPOL π allows identifying tissues with high absorption (e.g.,
336 pigment and axon) but without birefringence. These non-birefringent tissues appear dark gray.
337 This allows identifying the spatial relationship between collagen and non-birefringent tissues.
338 For example, IPOL π can visualize the relative displacement and deformation between collagen
339 and axon under stretch testing. For visualization, post-processing for IPOL π allows for making
340 the non-birefringent tissues invisible. In contrast, no information about these non-birefringent
341 tissues using conventional IPOL since they appear very dark in IPOL.

342 The IPOL π system setup is cheaper and simpler than the IPOL's. IPOL requires two pieces
343 of z-cut quartz, one right-handed and another left-handed. IPOL π only requires one, which can
344 be of either type. In our experience the left-handed z-cut quartz costs more than triple that of the
345 right-handed quartz. This alone should result in reduced costs. In addition, IPOL π can be
346 implemented with an imperfectly collimated light source. Polarization rotation through the z-cut
347 quartz is sensitive to the optical path length. In IPOL, the imaging system (e.g., dissecting
348 microscope) requires an extra light source collimator to make sure that a collimated light passes
349 through z-cut quartz in the illumination path. (Lee et al., 2020) This requirement increases the
350 system's complexity and cost. In IPOL π , the z-cut quartz can be placed directly into the imaging
351 path. Background artifacts are minimal since the light passing through the objective lens is
352 collimated. We acknowledge that when we set out to develop IPOL π our motivation was to
353 extend the color cycle to 180 degrees, which was essential to our applications. Identifying the
354 other strengths was somewhat fortuitous. It is not difficult now to imagine situations where these
355 strengths could be the primary motivation for choosing IPOL π over regular IPOL. An example of
356 the serendipity of science and the importance of research.

357 We have also shown how to establish quantitative color-angle and color-energy mappings
358 using an experimental calibration. The mapping technique can be applied to any regular color
359 cameras without automatic white balance control and single-color cameras with switching RGB
360 color filters. Note that all optical elements, such as the light source, optical filters and camera
361 parameters may impact the colors. Hence, the calibration is system specific. It is worth noting
362 that adjusting the brightness of the image should be based on the change in exposure time or
363 the use of a neutral density filter. Changing the power of the light source may change the

364 spectrum and thus affect the colors observed in IPOL π and in turn the mapping functions. Since
365 evaluating the interpolating functions at every color pixel takes time, we produced two
366 256x256x256 RGB lookup tables for orientation and energy inquiry, respectively, which
367 replaced time-consuming interpolation with an indexing operation. For a 20000x20000 mosaic
368 image, sufficient to include a full section of the posterior pole of the eye at 0.5 μ m/pixel
369 resolution, the computational time was reduced from 24 minutes to 6 seconds after using the
370 lookup table (1/240th of the time). The approach to quantifying local orientation and energy is
371 powerful and fast, as shown elsewhere in this paper. The color information at each pixel allows
372 us to characterize collagen fiber architecture without tracing individual fibers. Other imaging
373 techniques trace individual fibers through recognizing fiber edges (Cheng et al., 2018; Wu et al.,
374 2003), but these suffer in regions of high fiber density where the edges may be difficult to
375 discern. To avoid this problem it is common to increase the magnification, but this limits the field
376 of view. We acknowledge that the experimental calibration and quantitative method can be
377 improved. Although we demonstrated chicken tendon tissue sections as calibration samples,
378 they are imperfect. Commercial retarders or other synthetic materials may be necessary if finer
379 calibration is necessary. We have illustrated in Figure 3 that the HSV quantitative method is not
380 suitable for IPOL π , and have demonstrated a quantitative method in the RGB space based on
381 3D interpolation. Nevertheless, there may exist another color space whose parameters could be
382 simply used for IPOL π quantification.

383 It is important to consider the limitations of IPOL π . First, IPOL π , as presented in this work, is
384 based on transmitted light illumination, which requires thin samples. For soft tissues this often
385 means cutting them into thin sections, which limits the biomechanics applications. In the future it
386 may be possible to use structured light illumination to extend IPOL π to work with reflected light,
387 and thus be suitable for imaging thick tissues and potential for in vivo imaging. (Yang et al.,
388 2018a). Second, the diffraction artifacts from fiber edges in IPOL π lead to a sharply high energy
389 obtained after RGB color inquiry. Therefore, to build a color-energy interpolating function for
390 visualization and avoid artifacts, the energy in low-brightness pseudo calibrations was weighted
391 by the brightness. Third, tissue with selective absorption (e.g., stain) may affect the output color,
392 and thus induce an error in orientation and energy mapping. For example, hematoxylin and
393 eosin (H&E) stain is common in medical diagnosis. (Titford, 2005) Collagen appears strong pink
394 with H&E stain and its orientation color in IPOL π would be depressed by the stain. Fourth, the
395 colorful light of IPOL π contains information on all birefringent tissue components, including
396 various types of collagens and non-collagenous components, such as elastin and neural tissue

397 microtubules. (Waxman et al., 2022) Since the birefringence of collagen is substantially larger
398 than that of other birefringent elements in the eye (Inoué and Oldenbourg, 1998; Waxman et al.,
399 2021) we assumed that the majority of the polarized light interaction was from collagen. In
400 addition, we acknowledge that IPOL π cannot distinguish among various collagen types. The
401 ability to detect birefringence of other components could also be seen as a strength, as it allows
402 applying of IPOL π to study the structure and biomechanics of neural tissues. This could be
403 useful, for example, to study the optic nerve head of rodents, which have a glial, non-
404 collagenous lamina. (Tamm et al., 2017)

405 In conclusion, we present IPOL π as a label-free imaging technique for imaging collagen
406 tissues in the eye with high spatial, angular, and temporal resolutions. IPOL π optically encodes
407 collagen orientation and retardance in color at each pixel, and thus a color snapshot allows
408 visualization and quantification of collagen architecture. This study provides a novel imaging
409 modality to collagen microstructure and biomechanics in the eye, which could help understand
410 the role of collagen microstructure in eye physiology, aging, and in biomechanics-related
411 diseases.

412 **Acknowledgements**

413 **Disclosures:** Nothing to disclose.

414 **Funding:** Supported in part by National Institutes of Health R01-EY023966, R01-EY031708,
415 1S10RR028478, P30-EY008098 and T32-EY017271 (Bethesda, MD), the Eye and Ear
416 Foundation (Pittsburgh, PA), and Research to Prevent Blindness (unrestricted grant to UPMC
417 ophthalmology, and Stein innovation award to Sigal, IA).

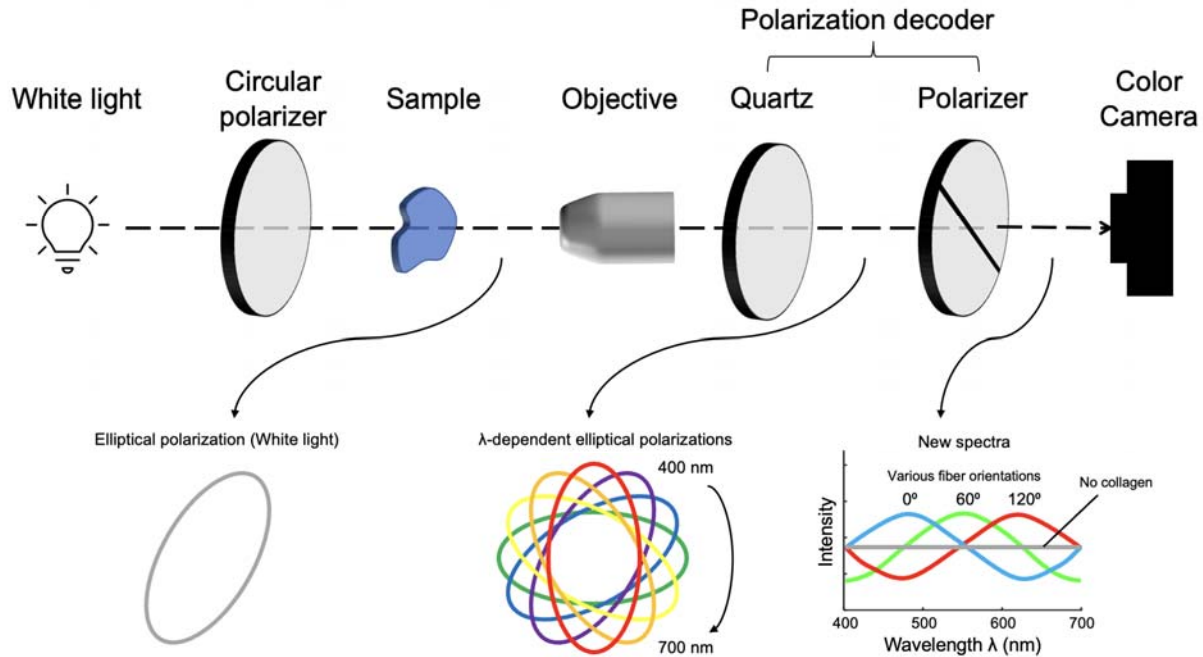
418

419 References

- 420 Amidror, I., 2002. Scattered data interpolation methods for electronic imaging systems: a
421 survey. *Journal of electronic imaging* 11, 157-176.
- 422 Axer, H., Axer, M., Krings, T., Keyserlingk, D.G.v., 2001. Quantitative estimation of 3-D fiber
423 course in gross histological sections of the human brain using polarized light. *Journal of*
424 *neuroscience methods* 105, 121-131.
- 425 Baumann, B., Rauscher, S., Glösmann, M., Götzinger, E., Pircher, M., Fialová, S., Gröger, M.,
426 Hitzemberger, C.K., 2014. Peripapillary rat sclera investigated in vivo with polarization-
427 sensitive optical coherence tomography. *Investigative ophthalmology & visual science*
428 55, 7686-7696.
- 429 Brazile, B.L., Hua, Y., Jan, N.-J., Wallace, J., Gogola, A., Sigal, I.A., 2018. Thin lamina cribrosa
430 beams have different collagen microstructure than thick beams. *Investigative*
431 *ophthalmology & visual science* 59, 4653-4661.
- 432 Canham, P.B., Finlay, H.M., Dixon, J.G., Ferguson, S.E., 1991. Layered collagen fabric of
433 cerebral aneurysms quantitatively assessed by the universal stage and polarized light
434 microscopy. *The Anatomical Record* 231, 579-592.
- 435 Cheng, F., Birder, L.A., Kullmann, F.A., Hornsby, J., Watton, P.N., Watkins, S., Thompson, M.,
436 Robertson, A.M., 2018. Layer-dependent role of collagen recruitment during loading of
437 the rat bladder wall. *Biomechanics and modeling in mechanobiology* 17, 403-417.
- 438 Cisek, R., Joseph, A., Harvey, M., Tokarz, D., 2021. Polarization-sensitive second harmonic
439 generation microscopy for investigations of diseased collagenous tissues. *Frontiers in*
440 *Physics* 9, 726996.
- 441 Collett, E., 2005. *Field guide to polarization*. Spie Bellingham, WA.
- 442 Coudrillier, B., Tian, J., Alexander, S., Myers, K.M., Quigley, H.A., Nguyen, T.D., 2012.
443 Biomechanics of the human posterior sclera: age-and glaucoma-related changes
444 measured using inflation testing. *Investigative ophthalmology & visual science* 53, 1714-
445 1728.
- 446 Diamant, J., Keller, A., Baer, E., Litt, M., Arridge, R., 1972. Collagen; ultrastructure and its
447 relation to mechanical properties as a function of ageing. *Proceedings of the Royal*
448 *Society of London. Series B. Biological Sciences* 180, 293-315.
- 449 Ethier, C.R., Johnson, M., Ruberti, J., 2004. Ocular biomechanics and biotransport. *Annu. Rev.*
450 *Biomed. Eng.* 6, 249-273.
- 451 Filas, B.A., Shah, N.S., Zhang, Q., Shui, Y.-B., Lake, S.P., Beebe, D.C., 2014. Quantitative
452 imaging of enzymatic vitreolysis-induced fiber remodeling. *Investigative Ophthalmology*
453 *& Visual Science* 55, 8626-8637.
- 454 Gogola, A., Jan, N.-J., Brazile, B., Lam, P., Lathrop, K.L., Chan, K.C., Sigal, I.A., 2018a. Spatial
455 patterns and age-related changes of the collagen crimp in the human cornea and sclera.
456 *Investigative ophthalmology & visual science* 59, 2987-2998.
- 457 Gogola, A., Jan, N.-J., Lathrop, K.L., Sigal, I.A., 2018b. Radial and circumferential collagen
458 fibers are a feature of the peripapillary sclera of human, monkey, pig, cow, goat, and
459 sheep. *Investigative ophthalmology & visual science* 59, 4763-4774.
- 460 Gruev, V., Perkins, R., York, T., 2010. CCD polarization imaging sensor with aluminum
461 nanowire optical filters. *Optics express* 18, 19087-19094.
- 462 Gusachenko, I., Tran, V., Housen, Y.G., Allain, J.-M., Schanne-Klein, M.-C., 2012.
463 Polarization-resolved second-harmonic generation in tendon upon mechanical
464 stretching. *Biophysical journal* 102, 2220-2229.
- 465 Higgins, M.D., 2010. Imaging birefringent minerals without extinction using circularly polarized
466 light. *The Canadian Mineralogist* 48, 231-235.
- 467 Inoué, S., Oldenbourg, R., 1998. Microtubule dynamics in mitotic spindle displayed by polarized
468 light microscopy. *Molecular biology of the cell* 9, 1603-1607.

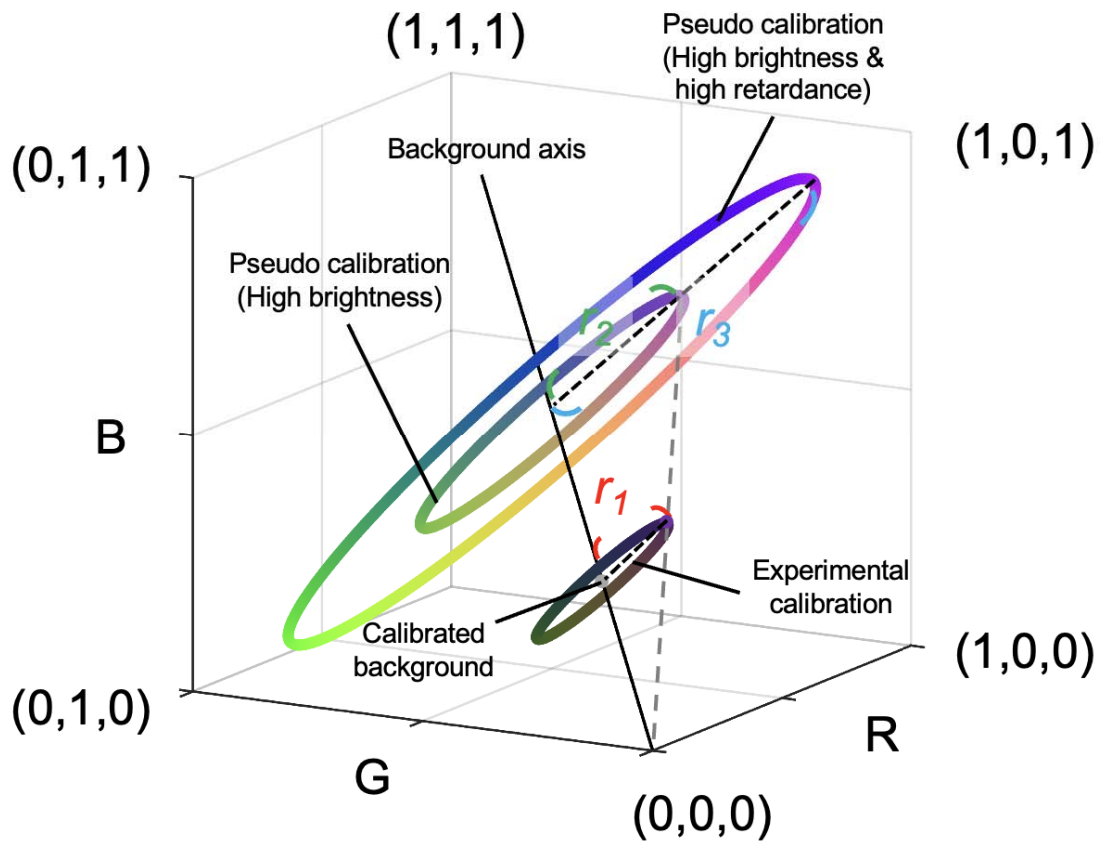
- 469 Jan, N.-J., Brazile, B.L., Hu, D., Grube, G., Wallace, J., Gogola, A., Sigal, I.A., 2018. Crimp
470 around the globe; patterns of collagen crimp across the corneoscleral shell.
471 *Experimental eye research* 172, 159-170.
- 472 Jan, N.-J., Gomez, C., Moed, S., Voorhees, A.P., Schuman, J.S., Bilonick, R.A., Sigal, I.A.,
473 2017a. Microstructural crimp of the lamina cribrosa and peripapillary sclera collagen
474 fibers. *Investigative ophthalmology & visual science* 58, 3378-3388.
- 475 Jan, N.-J., Grimm, J.L., Tran, H., Lathrop, K.L., Wollstein, G., Bilonick, R.A., Ishikawa, H.,
476 Kagemann, L., Schuman, J.S., Sigal, I.A., 2015a. Polarization microscopy for
477 characterizing fiber orientation of ocular tissues. *Biomedical optics express* 6, 4705-
478 4718.
- 479 Jan, N.-J., Lathrop, K., Sigal, I.A., 2017b. Collagen architecture of the posterior pole: high-
480 resolution wide field of view visualization and analysis using polarized light microscopy.
481 *Investigative ophthalmology & visual science* 58, 735-744.
- 482 Jan, N.-J., Lee, P.-Y., Wallace, J., Iasella, M., Gogola, A., Sigal, I.A., 2022. Stretch-Induced
483 Uncrimping of Equatorial Sclera Collagen Bundles. *bioRxiv*.
- 484 Jan, N.-J., Sigal, I.A., 2018. Collagen fiber recruitment: a microstructural basis for the nonlinear
485 response of the posterior pole of the eye to increases in intraocular pressure. *Acta*
486 *biomaterialia* 72, 295-305.
- 487 Jan, N.J., Grimm, J.L., Tran, H., Lathrop, K.L., Wollstein, G., Bilonick, R.A., Ishikawa, H.,
488 Kagemann, L., Schuman, J.S., Sigal, I.A., 2015b. Polarization microscopy for
489 characterizing fiber orientation of ocular tissues. *Biomed Opt Express* 6, 4705-4718.
- 490 Jan, N.J., Lathrop, K., Sigal, I.A., 2017c. Collagen Architecture of the Posterior Pole: High-
491 Resolution Wide Field of View Visualization and Analysis Using Polarized Light
492 Microscopy. *Invest Ophthalmol Vis Sci* 58, 735-744.
- 493 Kalwani, N.M., Ong, C.A., Lysaght, A.C., Haward, S.J., McKinley, G.H., Stankovic, K.M., 2013.
494 Quantitative polarized light microscopy of unstained mammalian cochlear sections.
495 *Journal of biomedical optics* 18, 026021.
- 496 Kaminsky, W., Gunn, E., Sours, R., Kahr, B., 2007. Simultaneous false-colour imaging of
497 birefringence, extinction and transmittance at camera speed. *Journal of microscopy* 228,
498 153-164.
- 499 Keefe, D., Tran, P., Pellegrini, C., Oldenbourg, R., 1997. Polarized light microscopy and digital
500 image processing identify a multilaminar structure of the hamster zona pellucida. *Human*
501 *reproduction (Oxford, England)* 12, 1250-1252.
- 502 Keikhosravi, A., Liu, Y., Drifka, C., Woo, K.M., Verma, A., Oldenbourg, R., Eliceiri, K.W., 2017.
503 Quantification of collagen organization in histopathology samples using liquid crystal
504 based polarization microscopy. *Biomedical optics express* 8, 4243-4256.
- 505 Keikhosravi, A., Shribak, M., Conklin, M.W., Liu, Y., Li, B., Loeffler, A., Levenson, R.M., Eliceiri,
506 K.W., 2021. Real-time polarization microscopy of fibrillar collagen in histopathology.
507 *Scientific reports* 11, 1-11.
- 508 Koike-Tani, M., Tani, T., Mehta, S.B., Verma, A., Oldenbourg, R., 2015. Polarized light
509 microscopy in reproductive and developmental biology. *Molecular reproduction and*
510 *development* 82, 548-562.
- 511 Lee, P.-Y., Yang, B., Hua, Y., Brazile, B., Ji, F., Zhu, Z., Fryc, G.A., Sigal, I.A., 2020. Instant
512 polarized light microscopy for real-time wide-field visualization of collagen architecture,
513 Label-free Biomedical Imaging and Sensing (LBIS) 2020. *International Society for Optics*
514 *and Photonics*, p. 112510Y.
- 515 Lee, P.-Y., Yang, B., Hua, Y., Waxman, S., Zhu, Z., Ji, F., Sigal, I.A., 2022. Real-time imaging of
516 optic nerve head collagen microstructure and biomechanics using instant polarized light
517 microscopy. *Experimental Eye Research* 217, 108967.

- 518 Mansfield, J.C., Winlove, C.P., Moger, J.J., Matcher, S.J., 2008. Collagen fiber arrangement in
519 normal and diseased cartilage studied by polarization sensitive nonlinear microscopy.
520 *Journal of biomedical optics* 13, 044020.
- 521 Mehta, S.B., Shribak, M., Oldenbourg, R., 2013. Polarized light imaging of birefringence and
522 diattenuation at high resolution and high sensitivity. *Journal of Optics* 15, 094007.
- 523 Schanda, J., 2007. Colorimetry: understanding the CIE system. John Wiley & Sons.
- 524 Schindelin, J., Arganda-Carreras, I., Frise, E., Kaynig, V., Longair, M., Pietzsch, T., Preibisch,
525 S., Rueden, C., Saalfeld, S., Schmid, B., 2012. Fiji: an open-source platform for
526 biological-image analysis. *Nature methods* 9, 676-682.
- 527 Shribak, M., Oldenbourg, R., 2003. Techniques for fast and sensitive measurements of two-
528 dimensional birefringence distributions. *Applied Optics* 42, 3009-3017.
- 529 Tamm, E.R., Ethier, C.R., Dowling, J.E., Downs, C., Ellisman, M.H., Fisher, S., Fortune, B.,
530 Fruttiger, M., Jakobs, T., Lewis, G., 2017. Biological aspects of axonal damage in
531 glaucoma: a brief review. *Experimental eye research* 157, 5-12.
- 532 Titford, M., 2005. The long history of hematoxylin. *Biotechnic & histochemistry* 80, 73-78.
- 533 Tower, T.T., Neidert, M.R., Tranquillo, R.T., 2002. Fiber alignment imaging during mechanical
534 testing of soft tissues. *Annals of biomedical engineering* 30, 1221-1233.
- 535 Waxman, S., Brazile, B.L., Yang, B., Lee, P.-Y., Hua, Y., Gogola, A.L., Lam, P., Voorhees, A.P.,
536 Rizzo III, J.F., Jakobs, T.C., 2021. Lamina cribrosa vessel and collagen beam networks
537 are distinct. *Experimental Eye Research*, 108916.
- 538 Waxman, S., Quinn, M.C., Donahue, C., Falo Jr, L.D., Sun, D., Jakobs, T.C., Sigal, I.A., 2022.
539 Individual Astrocyte Morphology in the Collagenous Lamina Cribrosa Revealed by
540 Multicolor DiOlistic Labeling. *bioRxiv*, 2022.2012. 2024.520184.
- 541 Whittaker, P., Przyklenk, K., 2009. Fibrin architecture in clots: a quantitative polarized light
542 microscopy analysis. *Blood Cells, Molecules, and Diseases* 42, 51-56.
- 543 Willemse, J., Gräfe, M.G., Verbraak, F.D., de Boer, J.F., 2020. In vivo 3D determination of
544 peripapillary scleral and retinal layer architecture using polarization-sensitive optical
545 coherence tomography. *Translational vision science & technology* 9, 21-21.
- 546 Wu, J., Rajwa, B., Filmer, D.L., Hoffmann, C.M., Yuan, B., Chiang, C.-S., Sturgis, J., Robinson,
547 J.P., 2003. Analysis of orientations of collagen fibers by novel fiber-tracking software.
548 *Microscopy and Microanalysis* 9, 574-580.
- 549 Yamanari, M., Nagase, S., Fukuda, S., Ishii, K., Tanaka, R., Yasui, T., Oshika, T., Miura, M.,
550 Yasuno, Y., 2014. Scleral birefringence as measured by polarization-sensitive optical
551 coherence tomography and ocular biometric parameters of human eyes in vivo.
552 *Biomedical optics express* 5, 1391-1402.
- 553 Yang, B., Brazile, B., Jan, N.-J., Hua, Y., Wei, J., Sigal, I.A., 2018a. Structured polarized light
554 microscopy for collagen fiber structure and orientation quantification in thick ocular
555 tissues. *Journal of biomedical optics* 23, 106001.
- 556 Yang, B., Jan, N.J., Brazile, B., Voorhees, A., Lathrop, K.L., Sigal, I.A., 2018b. Polarized light
557 microscopy for 3-dimensional mapping of collagen fiber architecture in ocular tissues.
558 *Journal of biophotonics* 11, e201700356.
- 559 Yang, B., Lee, P.Y., Hua, Y., Brazile, B., Waxman, S., Ji, F., Zhu, Z., Sigal, I.A., 2021. Instant
560 polarized light microscopy for imaging collagen microarchitecture and dynamics. *Journal*
561 *of Biophotonics* 14, e202000326.
- 562 York, T., Powell, S.B., Gao, S., Kahan, L., Charanya, T., Saha, D., Roberts, N.W., Cronin, T.W.,
563 Marshall, J., Achilefu, S., 2014. Bioinspired polarization imaging sensors: from circuits
564 and optics to signal processing algorithms and biomedical applications. *Proceedings of*
565 *the IEEE* 102, 1450-1469.



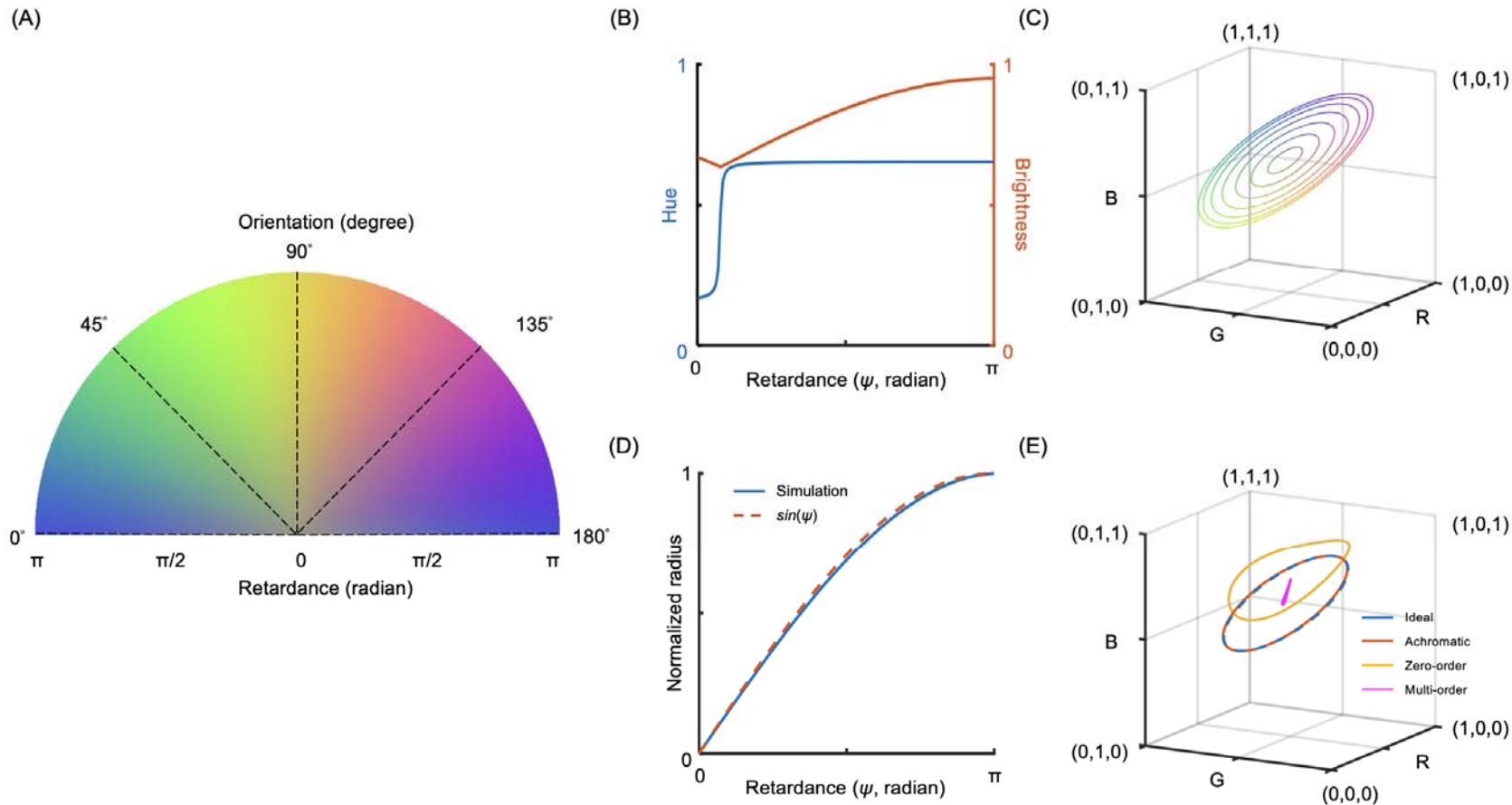
567

568 **Figure 1.** IPOL π imaging configuration. A circular polarizer and a polarization decoder are
569 retrofitted into the illumination and imaging paths, respectively. An alternative to the circular
570 polarizer is to use a linear polarizer followed by a quarter-wave plate whose slow and fast axes
571 are at 45°. The locations of the circular polarizer and the polarization decoder are swappable.
572 The polarization of the white light is converted into an elliptically polarized light by passing it
573 through the circular polarizer and the sample, where the orientation of the elliptical polarization
574 depends on local fiber orientation. A new spectrum is then generated after the elliptically
575 polarized light passed through the polarization decoder, and thus the output light is colorful. A
576 color camera acquires the colorful light to produce true-color images indicating collagen fiber
577 microstructure.



578

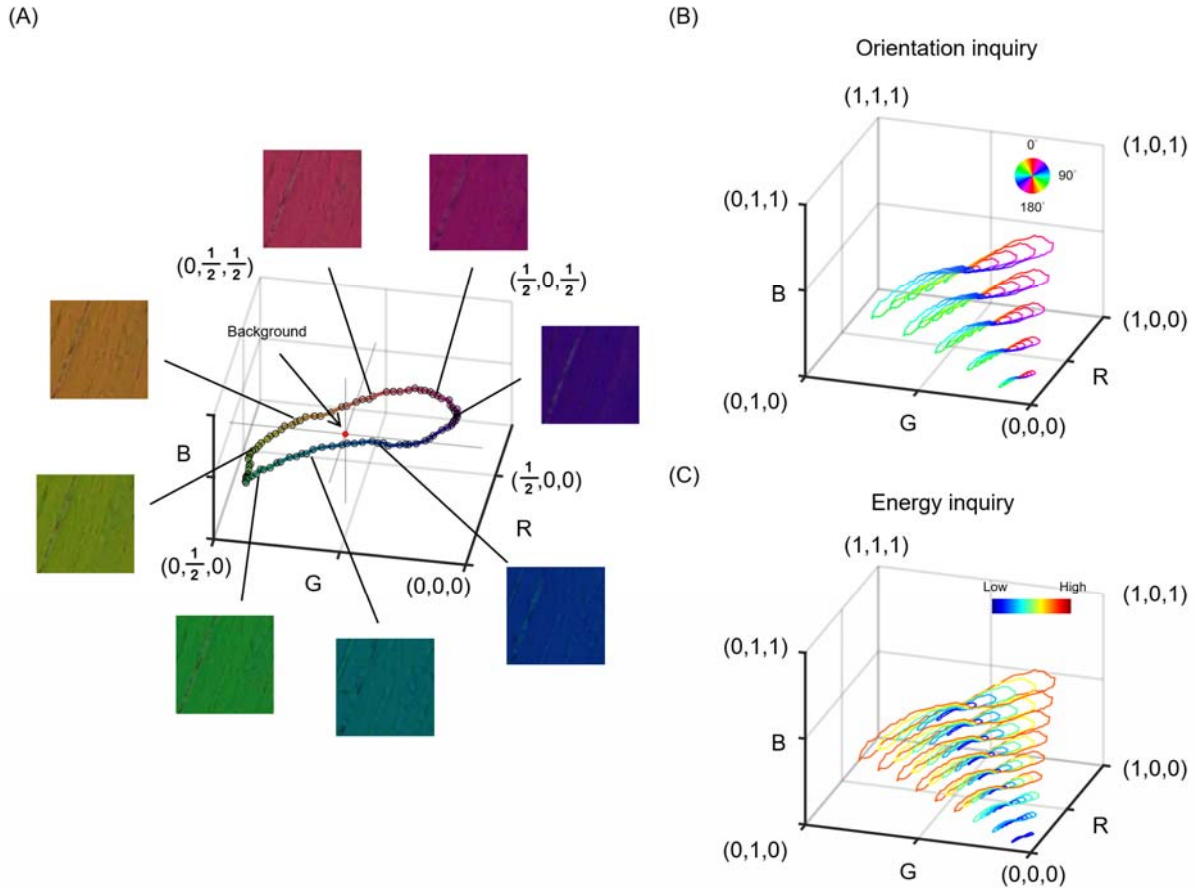
579 **Figure 2.** Generation of pseudo calibrations from the experimental calibration. An experimental
580 calibration created a ring with a calibrated background (i.e., central point) and a radius r_1 in the
581 color space. We defined the RGB distance between color on experimental calibration and
582 calibrated background (i.e., radius) as a unit of “energy”, which was related to retardance.
583 Pseudo calibrated rings were generated based on changes in brightness and energy. On one
584 hand, an increase in brightness results in an increase in RGB values in proportion due to
585 exposure time or tissue absorptance. For example, a pseudo calibration ring with a radius r_2
586 represents a higher exposure time or lower tissue absorption than the experimental calibrated
587 result. Although their radii are different, both have the same energy. On the other hand, an
588 increase in energy results in an increase in the radius of the calibrated ring in proportion. For
589 example, a sample generating a calibrated ring with a radius r_3 has higher energy than a sample
590 generating a calibrated ring with a radius r_2 . A combination of pseudo and experimental
591 calibrations was used to build interpolating functions for orientation and energy inquiry.



592

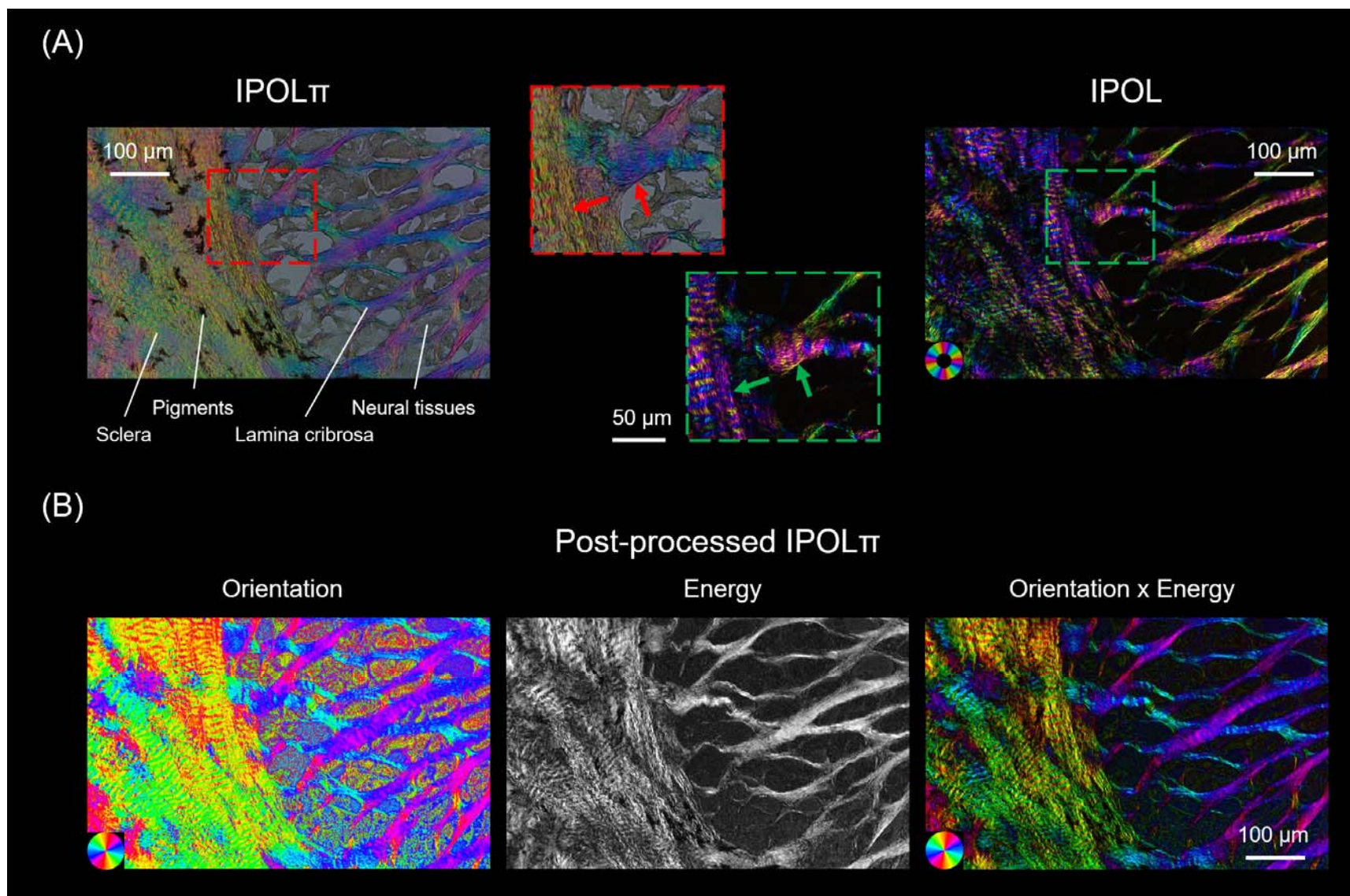
593 **Figure 3.** IPOL π simulation. (a) A simulated RGB color map of IPOL π based on an achromatic quarter waveplate covering fiber
 594 orientation angles from 0 to 180 degrees and retardance from 0 to π radians. (b) Extracting collagen oriented at a 0 degree from (a),
 595 the relationship between retardance and hue is not a constant and the relationship between retardance and brightness is not a
 596 strictly increasing function. (c) Extracting from (a), each simulated ring in the RGB color space corresponds to a collagen fiber with a
 597 constant retardance oriented at 0 to 180 degrees. The RGB curves with increased retardance present as concentric circles with

598 increased radiuses, whereas the RGB color for a sample with no retardance is located at the central point of the circle independent of
599 the orientations. (d) The normalized radius obtained from (c) follows the sine function of the retardance, which is equivalent with the
600 normalized “energy”. (e) Each simulated curve corresponds to IPOL π configured with a different type of quarter waveplate, to acquire
601 a collagen fiber oriented at 0 to 180 degrees. An RGB curve obtained from using an achromatic quarter waveplate is similar to the
602 curve obtained from using an ideal quarter waveplate. A distorted RGB ring obtained from a zero-order waveplate is still colorful, and
603 thus allows building an interpolating function that produces interpolated orientations and energies at inquiry RGBs. Using a multi-
604 order waveplate to build IPOL π lacks the ability to generate colorful images to visualize collagen microstructure.



605

606 **Figure 4.** The calibration curve of IPOL π in the RGB color space. (a) RGB values were
607 obtained from chicken tendon sections at different orientations using IPOL π . The calibration
608 curve was a ring, where the average of RGB values from all images was the background color
609 (red spot). (b) A combination of pseudo and experimental calibrations was used to build an
610 interpolating function that produced interpolated orientations at inquiry RGBs. Color represents
611 fiber orientation. (c) A combination of pseudo and experimental calibrations was used to build
612 an interpolating function that produced interpolated energies at inquiry RGBs. Color represents
613 energy. Note that the energy in low-brightness pseudo calibrations was weighted by the
614 brightness to avoid noise artifacts.



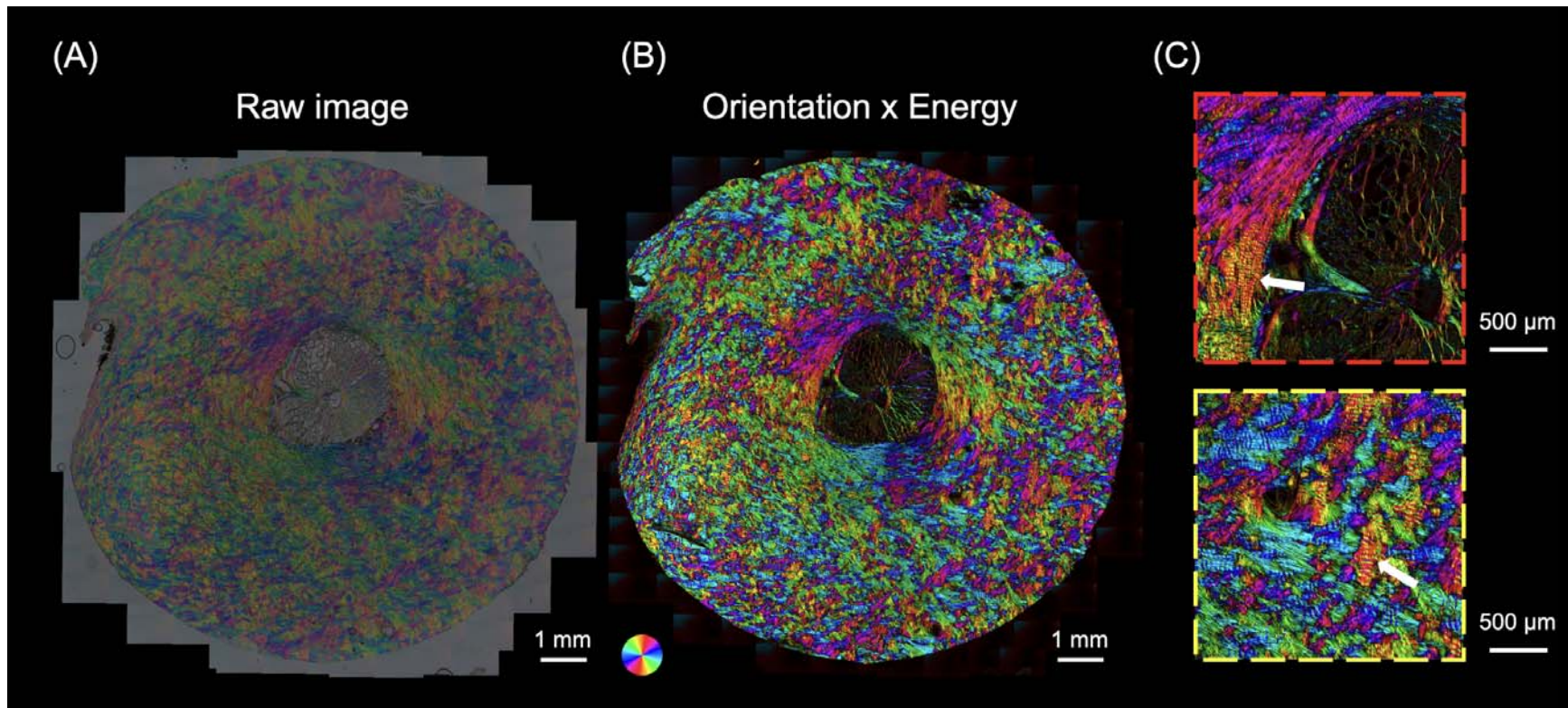
615

616

617

Figure 5. (A) Comparison between IPOL π (left) and IPOL (right) images as acquired of a section through the lamina cribrosa. The region is at the edge of the scleral canal where the sclera and lamina cribrosa meet. The IPOL π image has a grey background and

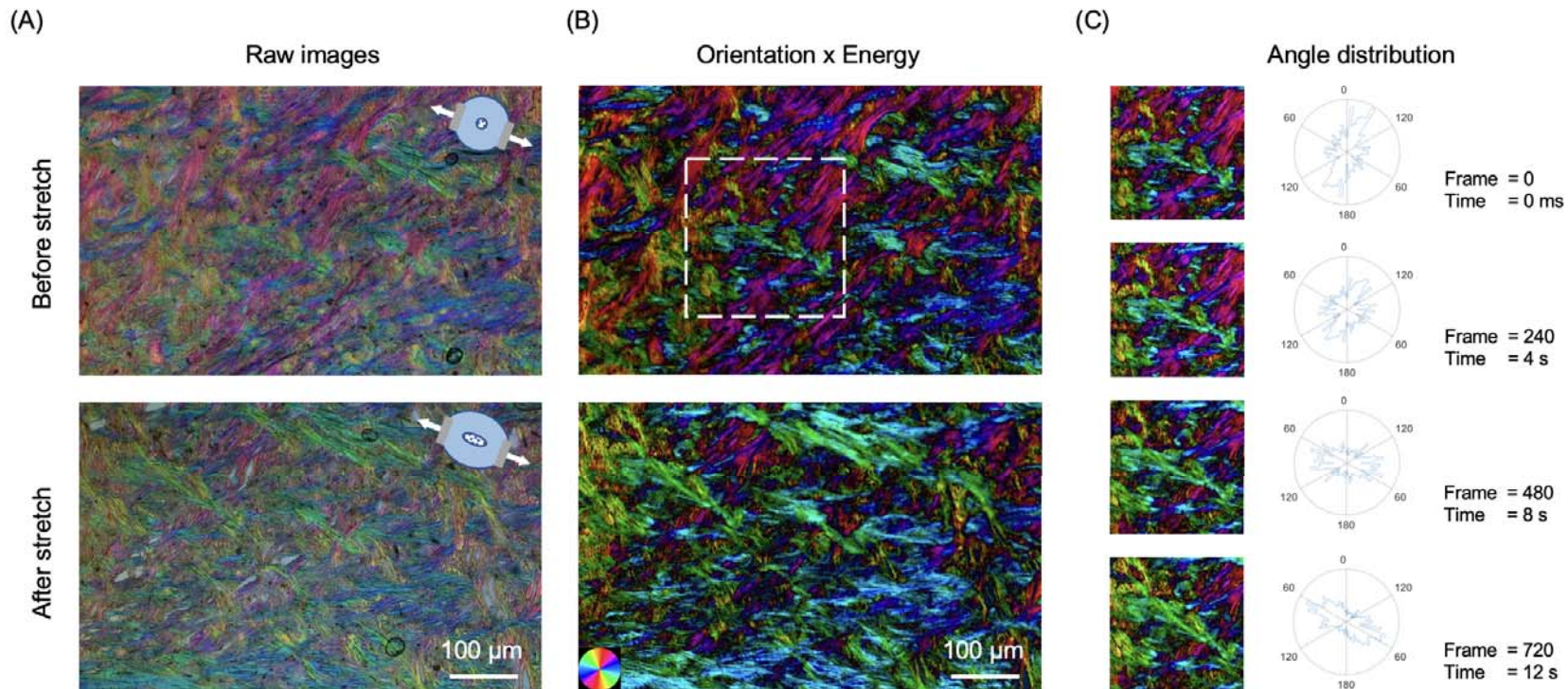
618 the colors low saturation. The dark regions correspond to pigments and the grey textured areas to neural tissues, primarily axons, but
619 also astrocytes and microglia. One of the major differences between IPOL π and IPOL is the orientation-encoded color cycle. The
620 IPOL π orientation-encoded color cycle is 180° and thus allows distinguishing the orientations of orthogonal fibers (red arrows) via
621 color. In contrast, the IPOL orientation-encoded color cycle is 90°, which indicates IPOL cannot directly identify the orientations of the
622 orthogonal fibers (green arrows) via color. (B) Post-processed IPOL π . Orientation and energy maps were extracted from the IPOL π
623 image using corresponding interpolating functions. For visualization, the “Orientation x Energy” image was obtained from the
624 orientation map of the collagen fibers with brightness scaled by the energy map. The color of the “Orientation x Energy” image had a
625 high contrast and saturation, and regions with low birefringence appear dark. This helps understand the architecture of collagen
626 fibers.



627

628 **Figure 6.** (a) A IPOL π image acquired as a mosaic of a coronal section from the optic nerve head of a sheep eye. (b) The post-
 629 processed color image was calculated from (a). The color disc on the top left-hand side of the image represents local fiber
 630 orientation, and the brightness in the image represents energy. (c) Close-up images from (b) shows interweaving in the peripapillary
 631 sclera (red box) and collagen beam networks in the lamina cribrosa (yellow box). The high-resolution image allows identifying crimp
 632 (white arrows), an important element of the microstructure for ocular biomechanics.

633



634

635 **Figure 7.** IPOL π can capture dynamic deformations of ocular tissues. (a) IPOL π images of an optic nerve head section before
636 stretch and after uniaxial stretch testing. The diagrams on the top right side indicate the stretch directions. (b) The corresponding
637 post-processed color images obtained from the orientation maps masked by the energy maps. (c) Time-sequence images and the
638 corresponding angle distributions from a small interest of region (white box). In the 720th frame, the high frequencies of fiber
639 orientations are close to the stretch directions. The angle distribution plots show the expected change in preferential fiber orientation
640 in the direction of stretch.